

Cite this: *Nanoscale Adv.*, 2019, 1, 4313

# Preparation and characterization of 0D Au NPs@3D BiOI nanoflower/2D NiO nanosheet array heterostructures and their application as a self-powered photoelectrochemical biosensing platform†

Qingzhi Han, Hanyu Wang, Yanting Qi, Dan Wu \* and Qin Wei 

In this work, we demonstrate that zero-dimensional Au nanoparticles (0D Au NPs)-decorated three-dimensional bismuth oxyiodide (BiOI) nanoflower (3D BiOI NFs)/two-dimensional nickel oxide (NiO) nanosheet array (2D NiO NSAs) hybrid nanostructures can be used as a self-powered cathodic photoelectrochemical (PEC) biosensing platform. The *in situ* formation of 3D BiOI NFs on 2D NiO NSAs was carried out by a chemical bath deposition method, while 0D Au NPs were coated on 3D BiOI NFs/2D NiO NSAs through a dip-coating method. Subsequently, glucose oxidase (GOD) as an enzyme model was immobilized on the surface of a Au@BiOI/NiO electrode via the adhesion of poly(diallyldimethylammonium chloride) (PDDA). The proposed heterostructure exhibited excellent PEC properties because the unique structure of the Au NPs@BiOI NFs/NiO NSAs increased the specific surface area, light harvesting ability and the surface plasmon resonance effect of the Au NPs. The system displayed high sensitivity toward glucose in the presence of an air-saturated electrolyte. At the optimum conditions, the biosensor showed a promising application for the self-powered cathodic PEC biosensing of glucose, with a dynamic linear range of  $1 \times 10^{-7}$  M to  $5 \times 10^{-2}$  M and a low limit of detection of  $8.71 \times 10^{-8}$  M. Moreover, the proposed self-powered PEC biosensor was evaluated for the determination of diluted glucose injections, with the results indicating the potential of the proposed biosensor for bioanalysis applications.

Received 22nd June 2019  
Accepted 4th September 2019

DOI: 10.1039/c9na00394k

rsc.li/nanoscale-advances

## Introduction

Since the first self-powered biosensor was reported by Katz E and Willner in 2001,<sup>1</sup> self-powered biosensors have received increasing attention. In a typical self-powered sensing platform, the sensor itself provides the power for the sensing device, eliminating the need for an external power supply.<sup>2–7</sup> In other words, a self-powered photoelectrochemical (PEC) biosensor is an integrated device with both an electronic power supply and biosensing function.<sup>8</sup> These characteristics are beneficial for the fabrication, economic efficiency, portability and miniaturization of the biosensors, thereby promoting self-powered biosensors as a powerful and promising candidate in the immunoassay field, especially for no-battery portable devices.<sup>9–11</sup> At present, with the development of nanomaterial science and nanotechnology, the structure, design and

application of semiconductors have received increasing attention. To obtain the desired PEC performance, the type, band gap size as well as the band matching of semiconductors require a judicious design and optimization.<sup>12–15</sup> Various heterostructures have been designed to expand the light utilization range or improve the electron ( $e^-$ )/hole ( $h^+$ ) separation efficiency,<sup>16</sup> such as: Au NPs@ZnO,<sup>17</sup> CdS/RGO/ZnO,<sup>3</sup> CdSe/ZnS/TiO<sub>2</sub>,<sup>18</sup> NiO/PbS<sup>12</sup> and C<sub>3</sub>N<sub>4</sub>/PbS.<sup>19</sup> Self-powered PEC biosensors can be divided into three major categories: p type/p-p heterostructure,<sup>12</sup> n type/n-n heterostructure<sup>3,4,17</sup> and photofuel cell type.<sup>20</sup>

P-type semiconductors, which are the opposite of n-type semiconductors, react more easily with electron acceptors (such as dissolved oxygen) than with electron donors (such as glutathione, ascorbic acid, and sodium sulfite) in the electrolyte, indicating their good potential for anti-interference from reducing substances.<sup>12,21,22</sup> In other words, p-type semiconductors are more stable than n-type semiconductors toward oxidation reactions.<sup>23</sup> As a popular p-type semiconductor, NiO (nickel oxide) has been widely used in the field of sensors, catalyzers and solar cells due to its good stability, unique electrochemical performance and excellent catalytic properties.<sup>20,24</sup>

Key Laboratory of Interfacial Reaction & Sensing Analysis in Universities of Shandong, University of Jinan, Jinan 250022, PR China. E-mail: wudan791108@163.com; Tel: +86-531-82767872

† Electronic supplementary information (ESI) available. See DOI: 10.1039/c9na00394k



BiOI (bismuth oxyiodide) is an ideal p-type photosensitizer with a narrow band gap ( $\sim 1.7$  eV) that possesses a wide visible light absorption range. When NiO and BiOI are combined, the photochemical properties are improved greatly.<sup>15</sup> We further added Au NPs to the surface of the NiO/BiOI heterostructure, which resulted in a unique structure and significantly improved photoelectrochemical activity.

In this work, we developed a novel self-powered PEC biosensor based on a Au@BiOI/NiO heterostructure. In detail, we decorated the three-dimensional BiOI nanoflowers (3D BiOI NFs) onto the surface of two-dimensional NiO nanosheet arrays (2D NiO NSAs) *via* the chemical bath deposition (CBD) technique.<sup>25</sup> The narrow band-gap p-type semiconductor BiOI ( $E_g = 1.7$  eV)<sup>22,25</sup> enlarged the light absorption range of NiO ( $E_g = 3.5$  eV)<sup>22</sup> and accelerated the  $e^-/h^+$  separation rate of the BiOI/NiO heterostructure. Subsequently, zero-dimensional Au nanoparticles (0D Au NPs) were introduced by a dip-coating method,<sup>26</sup> forming a Au@BiOI/NiO hybrid heterostructure. After glucose-oxidase (GOD) was fixed on the Au@BiOI/NiO/ITO electrodes, a self-powered PEC biosensor for glucose detection was successfully constructed, as shown in Scheme 1 below. In contrast with previous reports,<sup>15</sup> the proposed sensor exhibits the traditional  $O_2$ -dependent signal suppression mechanism and exhibits a high sensitivity. Owing to the unique 0D Au@3D BiOI/2D NiO hybrid nanostructure as well as the good conductivity and SPR effect of the Au NPs, compared with similar works,<sup>12,15</sup> the fabricated PEC biosensor showed better performance (lower LOD and wider detection range). Hence, the unique material combination and structural design are very important aspects for the improvement of the performance of the PEC biosensor.

## Experimental section

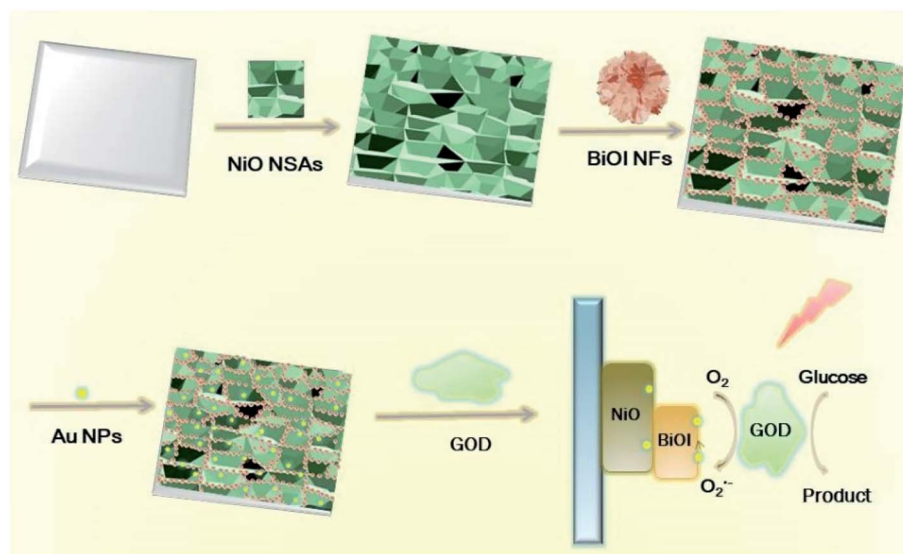
Chemicals and apparatus; synthesis of NiO, BiOI/NiO and Au@BiOI/NiO; SEM of excess BiOI CBD repeating cycles;

simulation parameters of the equivalent circuit components; comparison of various methods for the determination of glucose; and the determination of glucose in diluted glucose injections have been supplied in ESI.†

## Results and discussion

Characterization of the as-prepared materials. After  $Ni(OH)_2$  (morphologies are shown in Fig. S1†) was annealed at  $400^\circ C$  for 2 h (under an argon atmosphere), the obtained NiO (Fig. 1A and B (SEM); Fig. S2A† (TEM)) still maintained the NSAs structure. Fig. 1C illustrates that the XRD pattern of NiO was consistent with NiO (JCPDS PDF#44-1159-NiO), indicating the formation of NiO. A cross-sectional view demonstrated that the thickness of NiO on ITO is about  $2.4\ \mu m$  (Fig. 1D). As depicted by the SEM (Fig. 1E and F) and TEM images of BiOI/NiO (Fig. S2B†), the flower-like BiOI formed a uniform arrangement on the surface of the NiO NSAs, which would enlarge the specific surface area of NiO and provide additional enzyme loading sites. Moreover, the highly ordered heterostructure also benefited the electron transfer in the BiOI/NiO and further enhanced the photocurrent.<sup>3</sup>

A high-resolution transmission electron microscopy (HRTEM) image of the Au NPs is shown in Fig. 2A, which shows a diameter in the range of 12–14 nm (inset). Fig. 2B depicts the SEM image of the Au@BiOI/NiO hybrid nanostructure. As shown in the high magnification inset, the Au NPs are sparsely distributed on the surface of BiOI/NiO. The hybrid nanocomposites of the 0D Au NPs@BiOI/NiO is expected to have a high electron–hole separation efficiency as well as surface plasmon resonance (SPR) effect.<sup>27</sup> As shown in Fig. 2C, EDS analysis revealed that O, Bi, I, Au, and Ni elements existed in the sample, indicating that Au@BiOI/NiO was synthesized successfully.



Scheme 1 Preparation of 0D Au NPs modified 3D BiOI NF/2D NiO NSA heterostructures and its application for glucose detection.



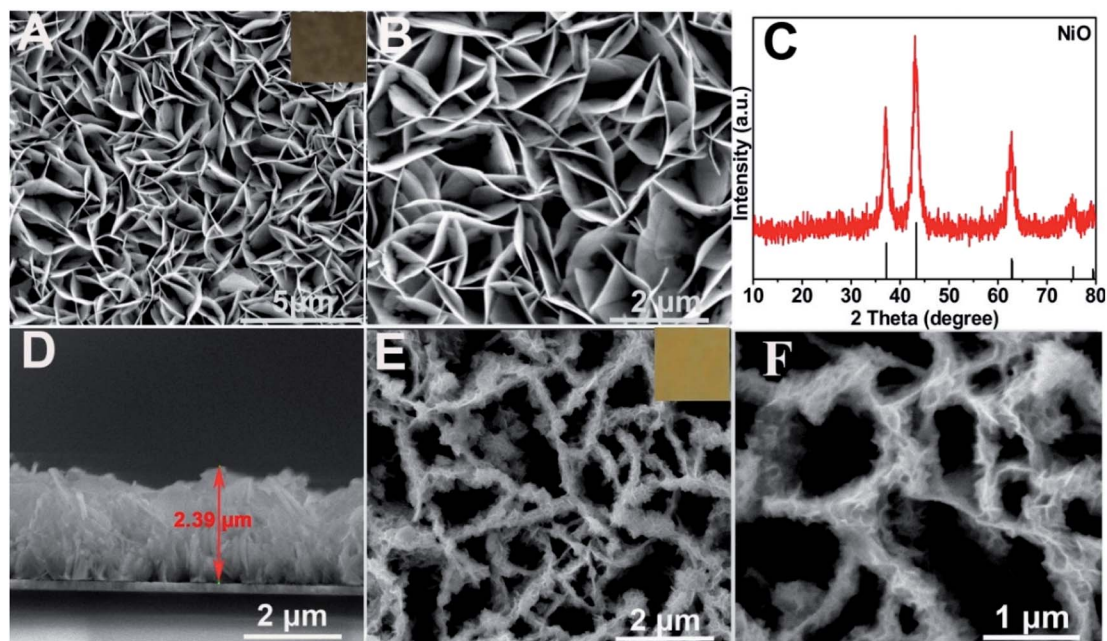


**Fig. 1** (A) SEM image of NiO NSAs. Inset is NiO-coated ITO. (B) High-magnification SEM image of NiO NSAs. (C) XRD pattern of the as-fabricated NiO NSAs. (D) The cross-sectional view of NiO/ITO electrode. (E) SEM image of NiO/BiOI nanostructure. Inset shows its color. (F) High-magnification SEM image of NiO/BiOI.

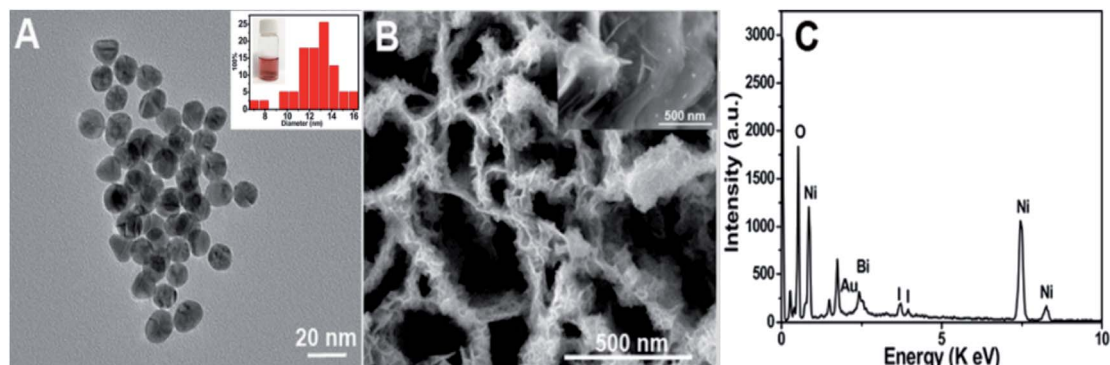


**Fig. 2** (A) HRTEM image of the as-synthesized Au NPs; inset: Au NPs size distribution and PVP-stabilized Au solution. (B) SEM image of Au NPs@BiOI NFs/NiO NSAs; inset shows the magnified view. (C) The corresponding EDS spectrum of the Au NPs@BiOI NFs/NiO NSAs electrode.

Fig. 3A–F offer the X-ray photoelectron spectroscopy (XPS) spectra of the Au@BiOI/NiO survey and the O 1s, Ni 2p, Bi 4f, I 3d and Au 4f regions. Obviously, the elements of Ni, I, O, Bi, and Au were detected in the XPS survey spectrum (Fig. 3A) in the range of 0–900 eV. C element (C 1s, 284.6 eV) was added as the internal standard in the spectrum. The asymmetric peak of the O 1s spectrum (Fig. 3B) illustrated that there are more than one chemical states of O. The peaks at 531.4 and 529.1 eV can be assigned to Ni–O, Bi–O, as well as the surface adsorbed oxygen, respectively. Fig. 3C depicts the XPS spectrum of Ni 2p, showing several peaks in the range of 851–882 eV. The peaks located at 853.1, 855.1, and 861.3 eV were attributed to Ni–O bonding. Notably, the peaks located at 853.5, 860.4 eV and 872.4, 878.7 eV can be attributed to Ni 2p<sub>3/2</sub> and Ni 2p<sub>1/2</sub> as well as the satellite peaks, respectively. As Fig. 3D suggests, the Bi 4f spectrum can

be fitted to two distinct peaks. The peaks centered at 158.6 and 164.0 eV are assigned to Bi 4f<sub>7/2</sub> and Bi 4f<sub>5/2</sub>, respectively, which can be ascribed to Bi<sup>3+</sup> in BiOI. Fig. 3E shows the XPS spectrum of I 3d with two different peaks in the binding energy range of 615–635 eV. Particularly, the peaks located at ~631 and ~619 eV were assigned to I 3d<sub>3/2</sub> and I 3d<sub>5/2</sub>, respectively. Two dissymmetrical binding energy peaks centered at 83.2 and 86.9 eV (Fig. 3F) were assigned to the binding energies of Au 4f<sub>7/2</sub> and Au 4f<sub>5/2</sub>, respectively. In addition, the deviation of the binding energies between these two peaks is 3.7 eV, according to previous literature on Au NPs existing in the metallic state.<sup>28</sup> Overall, the XPS spectra prove the successful synthesis of the Au@BiOI/NiO heterostructure.

To prove the formation of Au@NiO/BiOI, the as-prepared hybrid nanostructures were also characterized by Raman





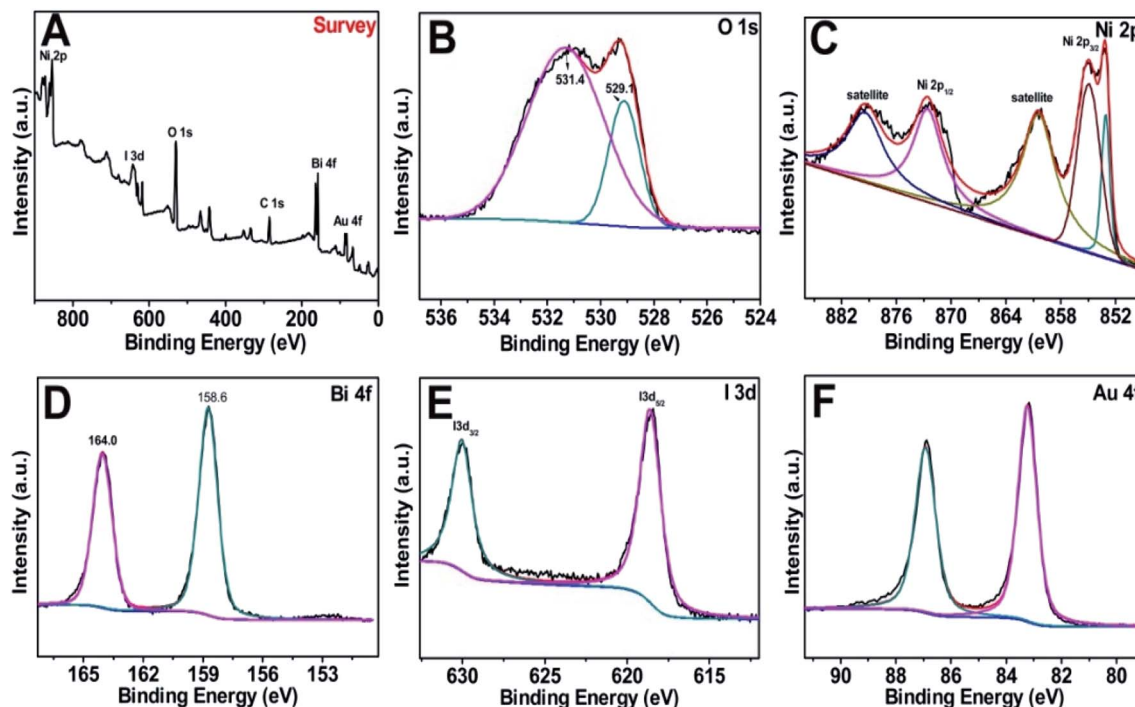


Fig. 3 (A) XPS survey of the as-fabricated Au@BiOI/NiO heterostructure and (B–F) high-resolution XPS spectra of O 1s, Ni 2p, Bi 4f, I 3d and Au 4f, respectively.

spectroscopy (Fig. 4A) and UV-vis absorption spectroscopy (Fig. 4B). For the Raman spectrum of NiO/BiOI (curve: a), the peaks at  $85\text{ cm}^{-1}$  and  $154\text{ cm}^{-1}$  were assigned to the Bi–I vibration of BiOI.<sup>29</sup> The peaks located at  $460\text{ cm}^{-1}$  could be attributed to the first-order transverse optical (TO) and longitudinal optical (LO) phonon modes of NiO.<sup>30</sup> The peaks located at  $\sim 1080\text{ cm}^{-1}$  were ascribed to the 2 LO of NiO.<sup>31</sup> Compared with curve a, after the addition of Au NPs (curve b), the Raman intensity was enhanced slightly, and the peaks were displaced, which could be attributed to the formation of Au@BiOI/NiO as well as the plasmonic effect of Au NPs. As depicted in Fig. 4B, the black curve is the UV-vis diffuse reflectance spectrum of pure NiO; after the addition of BiOI, the absorbance intensity

was enhanced in the range of 300–580 nm. With the further addition of Au NPs (Fig. 4B, blue curve), the absorption range was further enlarged. A small peak located at  $\sim 525\text{ nm}$  could be attributed to the plasmonic effect of Au NPs.<sup>27</sup>

#### Mechanism discussion of the constructed PEC biosensor

As presented in Scheme 2, a possible mechanism of the proposed PEC biosensor can be explained as follows. Under light irradiation, the photon-generated electrons of BiOI/NiO are transferred to the  $\text{O}_2$  in Tris–HCl to form  $\text{O}_2^-$ . Due to the SPR effect of the Au NPs, Au also provides electrons to the conduction band (CB) of BiOI and NiO, which further enhances

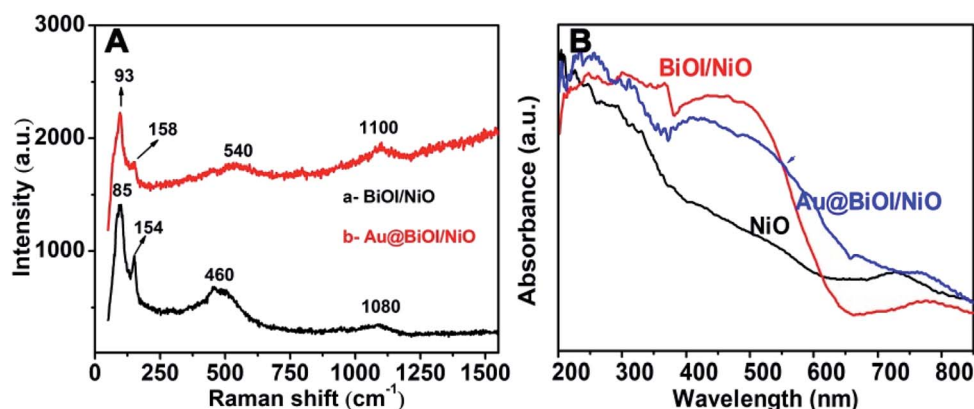
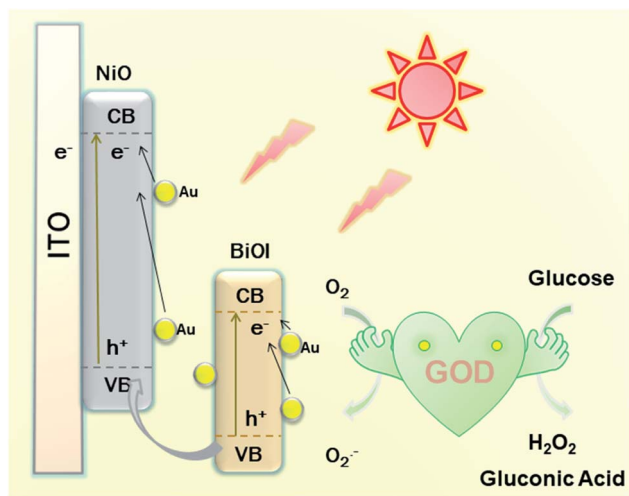


Fig. 4 (A) Raman spectra ( $\lambda_{\text{ex}} = 532\text{ nm}$ ) of the as-prepared NiO/BiOI/ITO and Au@NiO/BiOI/ITO samples. (B) UV-visible diffuse reflectance spectra of pure NiO, BiOI/NiO heterostructure and Au@BiOI/NiO hybrid nanocomposite.





Scheme 2 Schematic illustration of the mechanism for the self-powered PEC sensing platform.

the photocurrent performance of BiOI/NiO. Besides, the good conductivity of Au also accelerates the electron transfer rate. At the same time, the GOD consumes O<sub>2</sub> to decompose glucose, forming H<sub>2</sub>O<sub>2</sub> and gluconic acid. Owing to the O<sub>2</sub> consumption competition between the GOD and Au@BiOI/NiO, the cathodic photocurrent intensity of the self-powered biosensor is reduced. Compared with the report of Zhang *et al.*,<sup>15</sup> in this self-powered PEC sensing platform, the peroxidase-like catalytic activity of Bi<sup>i(+3-x)</sup> is not as strong as the O<sub>2</sub> consumption rate of the GOD. Consequently, in the proposed PEC self-powered sensing system, the decrease of photocurrent with the increasing concentration of glucose can be assigned to the decomposition of glucose in the electrolyte consumed by the dissolved oxygen (electron acceptors).

### PEC characterization of fabricated biosensor

To further explore the sensitivity of the Au@BiOI/NiO photocathode toward dissolved oxygen, we performed a contrast test (Fig. 5A). GOD can consume oxygen in the process of glucose

oxidation while generating H<sub>2</sub>O<sub>2</sub> and gluconic acid at the same time. 1 mM H<sub>2</sub>O<sub>2</sub> was added to the N<sub>2</sub> saturated buffer solution (blue curve). When compared with the photocurrent of the N<sub>2</sub> saturated buffer solution (red curve), no obvious change was found. As depicted in Fig. 5A, the air-saturated buffer solution (black curve) exhibited the highest photocurrent, which was larger than those of the N<sub>2</sub>-saturated buffer solution (red curve) and the N<sub>2</sub>-saturated (blue curve) buffer solution containing 1 mM H<sub>2</sub>O<sub>2</sub>. This results agreed with those from previous reports,<sup>32</sup> which demonstrated that in the proposed PEC sensing system, the dissolved O<sub>2</sub> has greater effect than the H<sub>2</sub>O<sub>2</sub> on the cathodic current. For comparison, the *I*-*V* curves of the Au@BiOI/NiO/ITO hybrid electrode were measured with light (black curve) as well as without light (red curve), and the results are depicted in Fig. 5B. Over the entire range (−0.2–0.2 V), as the applied potential increased, both curves increased as well. Under light illumination (black curve), the photocurrent density was larger than that without light, indicating that the PEC effect enhanced the generation of the cathodic photocurrent. Apparently, light is an important factor to actuate the proposed self-powered PEC sensing platform.

To obtain more detailed information about the matrix, the PEC performances of each layer in the matrix were also investigated. As depicted in Fig. 6A, under visible light irradiation, the NiO/ITO (curve a) showed a low current (∼−150 nA), while after the modification of BiOI (curve b), a significant increase in the photocurrent was observed. This could be attributed to the BiOI enhancing the light absorbance of NiO and sensitizing the wide bandgap of NiO. With the further modification of the Au NPs, the photocurrent reached about −16.4 μA. The reason might be the SPR effect of Au NPs as well as its good electron conductivity.<sup>27</sup> Curve d is the photocurrent response of GOD-Au@BiOI/NiO/ITO, which is lower than curve c (photocurrent response of Au@BiOI/NiO/ITO), indicating the successful modification of GOD (protein is non-conductive). Fig. 6B is the corresponding EIS Nyquist plots of Fig. 6A, and the plot shows that the semicircular part (electron transfer resistance) of the black curve (NiO/ITO) is smaller than that of the red curve (BiOI/NiO/ITO), indicating that BiOI was successfully modified. This is because the addition of semiconductor (BiOI) increased the electron transfer resistance

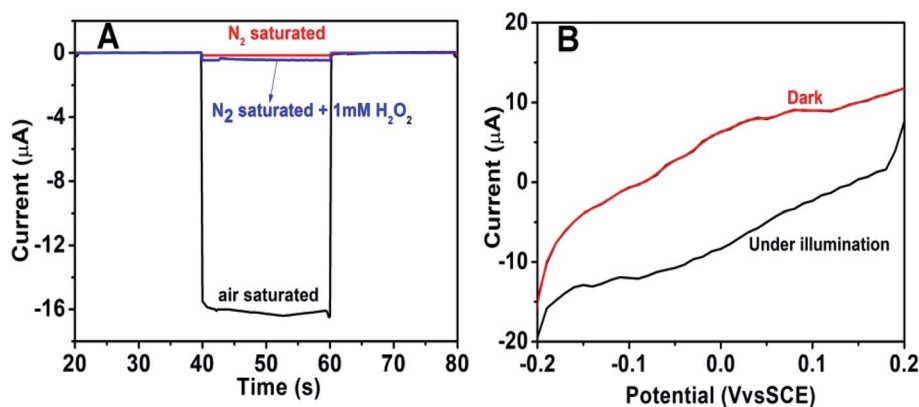


Fig. 5 (A) The photocurrent performance of Au@BiOI/NiO in air-saturated (black curve) and deaerated 0.1 M Tris-HCl solution (pH = 7.0) before (red curve) and after (blue curve) the injection of 1 mM H<sub>2</sub>O<sub>2</sub> (with 0 V applied potential vs. SCE and a LED light source). (B) The influence of light/no light on the *I*-*V* characteristic curves in the applied range (−0.2–0.2 V).



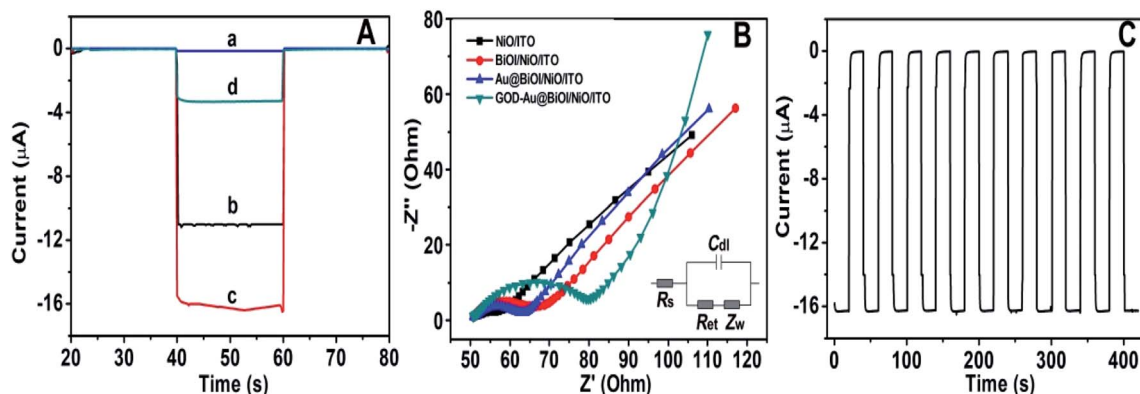


Fig. 6 (A) Photocurrent performance of (a) NiO/ITO (b) BiOI/NiO/ITO (c) Au@BiOI/NiO/ITO (d) GOD-Au@BiOI/NiO/ITO; the applied voltage is 0 V. (B) The corresponding EIS Nyquist plots (inset is the randles equivalent circuit of EIS). (C) PEC responses of the Au@BiOI/NiO/ITO electrode under several "on-off-on" irradiation cycles for 420 s (the applied voltage is 0 V).

( $R_{et}$ ). After the addition of the Au NPs (blue curve), the semicircular part was reduced, which could be attributed to the excellent conductivity of the Au NPs. When the GOD was fixed on the surface of Au@BiOI/NiO/ITO (green curve), the semicircular part was further enlarged, which could be attributed to the GOD (protein) blocking the transfer of electrons. The inset in Fig. 6B shows the equivalent circuit diagram of EIS, consisting of the solution resistance ( $R_s$ ),  $R_{et}$ , Warburg impedance ( $Z_w$ ) and the double layer capacitance ( $C_{dl}$ ). Amongst them,  $R_{et}$  is the most important indicator of the electrode's interface properties. The values of these parameters were simulated by ZsimpWin (simulation software) and are depicted in Table S1 (ESI<sup>†</sup>). Fig. 6C shows the output signal of the Au@BiOI/NiO/ITO electrode with repeated "on 20 s-off 20 s-on 20 s" cycles of light irradiation for 420 s. As can be seen, the signal curve of each independent cycle is homologous, which demonstrates the good signal output stability of the Au@BiOI/NiO/ITO electrode.

### Conditional selection for experiment

In order to acquire the optimum detectable signals, the external experimental conditions for the self-powered PEC platform need to be investigated. First, we studied the effect of the number of CBD cycles on the photocurrent response of the self-powered

sensing system. As depicted in Fig. 7A, when the number of CBD cycles was 4, the BiOI/NiO in Tris-HCl exhibited the biggest photocurrent ( $\sim -10.5 \mu\text{A}$ ). With the CBD cycles further increased, the photocurrent decreased instead; this could be attributed to the difference in size, shape and disordered distribution of excess BiOI impeding the electron transfer rate. As shown in Fig. S3,<sup>†</sup> with the increase in the number of CBD cycles, the BiOI gradually grows on the surface of NiO. When the number of CBD cycles exceeds 4, the morphology of the BiOI/NiO becomes disorganized. Thus, 4 cycles were used for the deposition of BiOI.

The number of dip-coating times for the Au NPs was also optimized. As shown in Fig. 7B, as the dipping times increased, the photocurrent gradually increased and then reached a maximum value ( $\sim -16.4 \mu\text{A}$ ) after 4 dip-coating times; subsequently, it reduced gradually. The reason might be that the excess Au NPs accelerated the  $e^-/h^+$  recombination rate and reduced the photocurrent. For the best PEC performance, 4 dipping times was chosen for the decoration of the Au NPs.

### Characterization of analytical performance

Under the optimized experimental conditions, we investigated the analytical performance of the self-powered PEC biosensor by detecting glucose at different concentrations. The

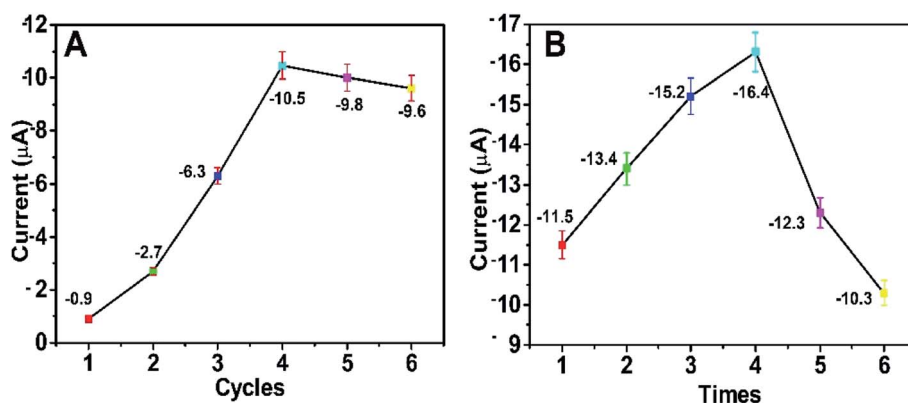


Fig. 7 Effects of (A) the number of BiOI CBD repeating cycles and (B) the number of Au NP dip-coating times on the PEC performance of the self-powered platform. The applied voltage is 0 V.



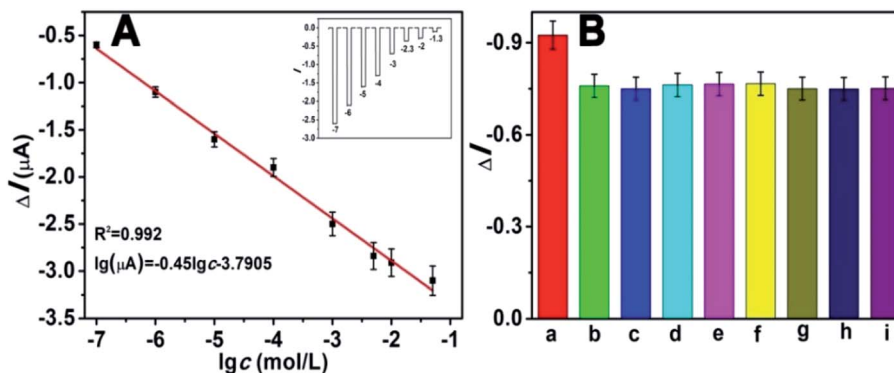


Fig. 8 (A) The photocurrent decrease ( $\Delta I = I_0 - I$ ) of the GOD-modified Au@BiOI/NiO/ITO electrode vs.  $-\log c_{\text{glucose}}$ .  $I_0$  and  $I$  are the photocurrents of the GOD-modified electrodes pre- and post-reaction with glucose, respectively. Inset is the corresponding photocurrent response for different concentrations of glucose; the applied voltage is 0 V. (B) Effect of added substances (1 mM): (a) glucose, (b) NaCl, (c) KCl, (d) ascorbic acid (AA), (e) dopamine, (f) urea, (g) L-valine, (h) L-lysine, (i) mixture (glucose + (b–h)), on the photocurrent response of the GOD-Au@BiOI/NiO/ITO electrode.

photocurrent response of the biosensor changed regularly toward the concentration of glucose. Fig. 8A depicts that the photocurrent decreased with the increasing concentration of glucose. As mentioned previously, as the concentration of glucose increased, the competition between the photocathode and GOD also increased. The higher the concentration of glucose, the more dissolved  $O_2$  (electron acceptors) is consumed by GOD. As depicted in the diagram, the photocurrent response linearly decreased with the increasing logarithm of glucose in the range of  $1 \times 10^{-7}$  to  $5 \times 10^{-2}$  M. The calibration equation was  $\Delta I = -0.45 \log c - 3.7905$ , with a correlation coefficient of 0.992. Estimated according to the previous method of a signal-to-noise ratio of 3 : 1 ( $S/N = 3$ ),<sup>13,33</sup> the limit of detection (LOD) was  $8.71 \times 10^{-8}$  M. Compared with many previous reports for the determination of glucose (Table S2†), our work showed a wider dynamic linear range and lower LOD, indicating its advance in glucose analysis. The inset of Fig. 8A shows the corresponding photocurrent response. The selectivity of the proposed PEC biosensor was determined, and the results are shown in Fig. 8B. There were several potentially interfering species that were used for the test, including NaCl, dopamine and several amino acids. Except for the interfering substances, all the tests were operated under identical experimental conditions. In this anti-interference experiment, the concentrations of glucose and the interfering species both were 1 mM. Apparently except for the glucose (bar a), the other substances had no distinct influence, indicating the excellent selectivity of this self-powered PEC biosensor.

To evaluate the reproducibility of this self-powered sensing platform, we performed an intra-assay and inter-assay test. The intra-assay test was conducted by testing five times with concentrations of 3 mM and 6 mM glucose, from which the obtained relative standard deviation (RSD) values were 4.7% and 4.3%, respectively. Under exactly the same conditions, five electrodes were used to measure one sample for the inter-assay, and the resulting RSD values were 4.9% and 5.1%, respectively. These results indicated the applicability of the proposed system for future utilization. In order to prove the feasibility of the GOD-Au@BiOI/NiO electrode for routine analysis, the proposed

biosensor was used to detect diluted glucose injections. As depicted in Table S3,† the diluted glucose injections were measured by combining standard samples with different glucose levels for the recovery experiment. The obtained experimental results demonstrated that the proposed PEC biosensor has acceptable accuracy, which indicates its potential for biological applications.

## Conclusions

In summary, we developed a novel self-powered PEC biosensing platform based on a 0D Au@3D BiOI/2D NiO/ITO photocathode, and we described the construction and characterization of the hybrid nanocomposite. The obtained experimental results indicated the ideal coupling between the 0D Au NPs QDs, 3D BiOI NFs and 2D NiO NSAs. Owing to the sensitization effect of BiOI as well as the SPR effect and good conductivity of the Au NPs, the constructed 0D Au@3D BiOI/2D NiO/ITO photocathode showed excellent PEC activities and oxygen sensitivity. The self-powered PEC sensing platform also exhibited high sensitivity and good anti-interference when it was used to detect glucose *in vitro*. Besides, the fabricated PEC biosensor was successfully used for the detection of glucose injections. The results indicate that the proposed Au@BiOI/NiO photocathode has promising prospects for self-powered PEC biosensing devices. More generally, this work proved that heterostructure and material combination design is still an efficient method for improving the performance of PEC biosensing devices.

## Conflicts of interest

The authors declare no competing financial interest.

## Acknowledgements

We are very grateful to National Natural Science Foundation of China (Grant no. 21775054), the Natural Science Foundation of Shandong Province (Grant no. ZR2016JL013).





## Notes and references

- 1 E. Katz, A. F. Buckmann and I. Willner, *J. Am. Chem. Soc.*, 2001, **123**, 10752–10753.
- 2 M. Grattieri and S. D. Minter, *ACS Sens.*, 2018, **3**, 44–53.
- 3 K. Zhao, X. Yan, Y. Gu, Z. Kang, Z. Bai, S. Cao, Y. Liu, X. Zhang and Y. Zhang, *Small*, 2016, **12**, 245–251.
- 4 Z. Kang, Y. Gu, X. Yan, Z. Bai, Y. Liu, S. Liu, X. Zhang, Z. Zhang, X. Zhang and Y. Zhang, *Biosens. Bioelectron.*, 2015, **64**, 499–504.
- 5 B. Çakıroğlu and M. Özacar, *Biosens. Bioelectron.*, 2018, **119**, 34–41.
- 6 W. W. Zhao, J. J. Xu and H. Y. Chen, *Chem. Soc. Rev.*, 2015, **44**, 729–741.
- 7 C. Li, C. Han, Y. Zhang, Z. Zang, M. Wang, X. Tang and J. Du, *Sol. Energy Mater. Sol. Cells*, 2017, **172**, 341–346.
- 8 A. Devadoss, P. Sudhagar, C. Terashima, K. Nakata and A. Fujishima, *J. Photochem. Photobiol., C*, 2015, **24**, 43–63.
- 9 B. Peng, L. Tang, G. Zeng, S. Fang, X. Ouyang, B. Long, Y. Zhou, Y. Deng, Y. Liu and J. Wang, *Biosens. Bioelectron.*, 2018, **121**, 19–26.
- 10 I. C. Wu, Y. H. Weng, M. Y. Lu, C. P. Jen, V. E. Fedorov, W. C. Chen, M. T. Wu, C. T. Kuo and H. C. Wang, *Opt. Express*, 2017, **25**, 7689–7706.
- 11 K. Yan, Y. Yang, Y. Zhu and J. Zhang, *Anal. Chem.*, 2017, **89**, 8599–8603.
- 12 W. X. Dai, L. Zhang, W. W. Zhao, X. D. Yu, J. J. Xu and H. Y. Chen, *Anal. Chem.*, 2017, **89**, 8070–8078.
- 13 Q. Han, R. Wang, B. Xing, H. Chi, D. Wu and Q. Wei, *Biosens. Bioelectron.*, 2018, **106**, 7–13.
- 14 Q. Han, R. Wang, B. Xing, T. Zhang, M. S. Khan, D. Wu and Q. Wei, *Biosens. Bioelectron.*, 2018, **99**, 493–499.
- 15 L. Zhang, Y. F. Ruan, Y. Y. Liang, W. W. Zhao, X. D. Yu, J. J. Xu and H. Y. Chen, *ACS Appl. Mater. Interfaces*, 2018, **10**, 3372–3379.
- 16 K. Kim, H. Kim, H. Jang, J. Park, G.-Y. Jung and M. G. Kim, *ACS Appl. Mater. Interfaces*, 2018, **10**, 39487–39493.
- 17 Z. Kang, X. Yan, Y. Wang, Y. Zhao, Z. Bai, Y. Liu, K. Zhao, S. Cao and Y. Zhang, *Nano Res.*, 2016, **9**, 344–352.
- 18 G. K. C. dos Santos, F. G. S. da Silva, S. Yotsumoto Neto, W. T. P. dos Santos, R. de Cássia Silva Luz and F. S. Damos, *Electroanalysis*, 2018, **30**, 1750–1756.
- 19 R. Li, Y. Zhang, W. Tu and Z. Dai, *ACS Appl. Mater. Interfaces*, 2017, **9**, 22289–22297.
- 20 K. Yan, Y. Yang, O. K. Okoth, L. Cheng and J. Zhang, *Anal. Chem.*, 2016, **88**, 6140–6144.
- 21 M. G. Kibria, F. A. Chowdhury, S. Zhao, B. Alotaibi, M. L. Trudeau, H. Guo and Z. Mi, *Nat. Commun.*, 2015, **6**, 6797.
- 22 L. Yosefi and M. Haghghi, *Appl. Catal., B*, 2018, **220**, 367–378.
- 23 G. C. Fan, X. M. Shi, J. R. Zhang and J. J. Zhu, *Anal. Chem.*, 2016, **88**, 10352–10356.
- 24 Y. Ku, C. N. Lin and W. M. Hou, *J. Mol. Catal. A: Chem.*, 2011, **349**, 20–27.
- 25 Y. Zhang, Q. Pei, J. Liang, T. Feng, X. Zhou, H. Mao, W. Zhang, Y. Hisaeda and X. M. Song, *Langmuir*, 2015, **31**, 10279–10284.
- 26 Y. Dou, J. Zhou, A. Zhou, J. R. Li and Z. Nie, *J. Mater. Chem. A*, 2017, **5**, 19491–19498.
- 27 S. Eustis and M. A. El Sayed, *Chem. Soc. Rev.*, 2006, **35**, 209–217.
- 28 J. Wu, C. Luo, D. Li, Q. Fu and C. Pan, *J. Mater. Sci.*, 2017, **52**, 1285–1295.
- 29 K. H. Ye, Z. Chai, J. Gu, X. Yu, C. Zhao, Y. Zhang and W. Mai, *Nano Energy*, 2015, **18**, 222–231.
- 30 W. Wang, Y. Liu, C. Xu, C. Zheng and G. Wang, *Chem. Phys. Lett.*, 2002, **362**, 119–122.
- 31 R. E. Dietz, G. I. Parisot and A. E. Meixner, *Phys. Rev. B: Solid State*, 1971, **4**, 2302–2310.
- 32 W. W. Zhao, J. Wang, Y. C. Zhu, J. J. Xu and H. Y. Chen, *Anal. Chem.*, 2015, **87**, 9520–9531.
- 33 Y. Liu, K. Yan and J. Zhang, *ACS Appl. Mater. Interfaces*, 2016, **8**, 28255–28264.

